Check for updates

Optics EXPRESS

Field-position dependent apodization in dark-field digital holographic microscopy for semiconductor metrology

TAMAR VAN GARDINGEN-CROMWIJK,[1,2,*] MANASHEE ADHIKARY,[1,2] CHRISTOS MESSINIS,[3] SANDER KONIJNENBERG,[3] WIM COENE,[3] STEFAN WITTE,[1,2] JOHANNES F. DE BOER,[1] AND ARIE DEN BOEF[1,2,3]

[1] *Department of Physics and Astronomy, and LaserLaB, Vrije Universiteit, De Boelelaan 1081, 1081 HV Amsterdam, The Netherlands*
[2] *Advanced Research Center for Nanolithography (ARCNL), Science Park 106, 1098 XG Amsterdam, The Netherlands*
[3] *ASML Netherlands B.V., De Run 6501, 5504 DR Veldhoven, The Netherlands*
[*] *t.cromwijk@arcnl.nl*

Abstract: Measuring overlay between two layers of semiconductor devices is a crucial step during electronic chip fabrication. We present dark-field digital holographic microscopy that addresses various overlay metrology challenges that are encountered in the semiconductor industry. We present measurement results that show that the point-spread function of our microscope depends on the position in the field-of-view. We will show that this novel observation can be explained by a combination of the finite bandwidth of the light source and a wavelength-dependent focal length of the imaging lens. Moreover, we will also present additional experimental data that supports our theoretical understanding. Finally, we will propose solutions that reduce this effect to acceptable levels.

© 2022 Optica Publishing Group under the terms of the Optica Open Access Publishing Agreement

1. Introduction

Over the past 55 years Moore's Law has been the leading principle in the semiconductor industry [1]. In order to keep pace with Moore's Law for another few decades, lithography should continue to enable the printing of even smaller features. As a consequence, significant improvements in optical metrology are required. Optical wafer metrology plays an important role in the manufacturing process of integrated circuits. A crucial step during the fabrication is measuring the lateral alignment with respect to the previous wafer layer in the multilayer stack. This metrology step is called overlay (OV) metrology and is of importance for optimizing and controlling the fabrication process and detecting problematic wafers early. Recently, dark-field digital holographic microscopy (df-DHM) has been proposed as a promising new technique to address the growing challenges of OV metrology in the semiconductor industry [2–6].

DHM acquires the coherent superposition of a reference beam and an object beam on an image sensor. From the recorded interference pattern (hologram) the complex-valued object field can be retrieved, which gives access to amplitude and phase of the object [7]. The measured complex object field in combination with computational imaging techniques, allows us to digitally correct for imperfections in the optical system.

The concept of our df-DHM setup is presented in Fig. 1, where dedicated metrology targets are measured using a diffraction-based overlay (DBO) metrology technique [8–10]. Here the intensity difference between $+1^{st}$ and -1st diffraction orders, coming from two biased overlapping gratings, scales linearly with the OV error. The image field can be reconstructed from the hologram using fast Fourier transform techniques as shown in Fig. 1(b), (c), and (d).

#476157 https://doi.org/10.1364/OE.476157
Journal © 2023 Received 22 Sep 2022; revised 28 Nov 2022; accepted 29 Nov 2022; published 21 Dec 2022

Optics EXPRESS

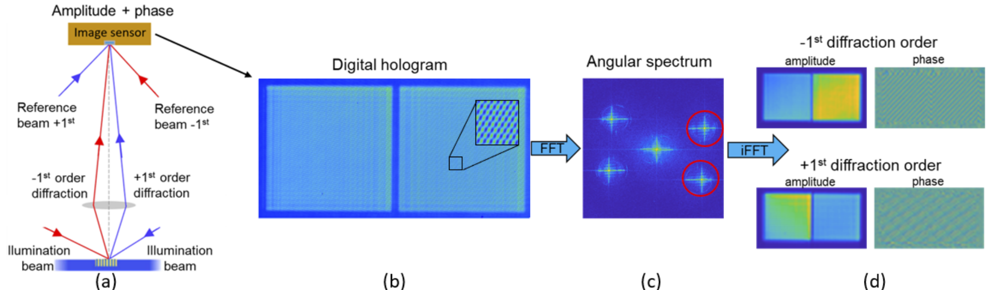

Fig. 1. (a) A schematic representation of the working principle of our df-DHM setup. The sample is illuminated with two oblique illumination beams. The diffracted $+1^{st}$ and -1st orders are captured by the imaging lens and coherently mixed with their respective reference beams, resulting in two overlapping holograms at the image plane, (b). By Fourier transforming the hologram we get the angular spectrum and the field back-propagated to the pupil plane, as shown in (c). The illumination branches have different azimuthal angles with respect to the reference arms resulting in a 90° angle difference. Performing an inverse Fourier transform of one side band from each arm (circled in red), results in the reconstruction of the complex field, retrieving the phase and amplitude from each branch, given in (d).

Metrology targets typically have dimensions of about $10 \times 10\ \mu m^2$ and are often surrounded by other structures. Due to the finite imaging resolution of the optical sensor, optical crosstalk can occur where light from the surrounding structures leaks into the image of the metrology target. This effect can impact the quality of metrology and while apodization techniques can be used to minimize these errors, a near-perfect aberration-free imaging performance with a localized point-spread function (PSF) is required. In earlier work we have already reported about the aberration-correction capabilities of our df-DHM concept [5] and the use of digital apodization to optimize the localization of the PSF [6]. In this paper, we will show that in our df-DHM concept the finite bandwidth of our light source in combination with a wavelength-dependent focal length of our imaging lens introduces a field-position dependent spurious apodization that leads to a field-position dependent aberration-corrected PSF. A schematic presentation of the field-position dependent PSF that we observed with our df-DHM setup is shown in Fig. 2, demonstrating the importance of a well defined PSF.

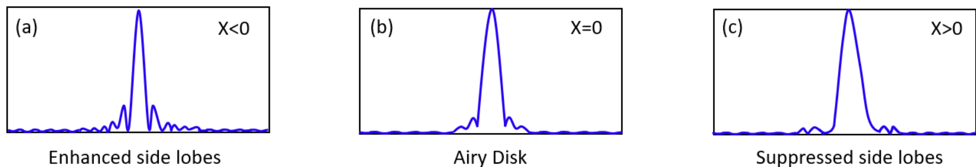

Fig. 2. Schematic representation of a field-position dependent amplitude modulated point-spread function. (a) cross section of a PSF at left side of the field ($X<0$) where the side lobes are enhanced resulting in more crosstalk and a higher resolution (b) PSF that we observe in the center of the field ($X=0$). Here the PSF shape closely resembles an ideal Airy Disk. (c) cross section of an apodized PSF that we observe at the right side of the field ($X>0$) suppressing the high frequencies, resulting in less crosstalk and a lower resolution.

A gradual broadening of the central peak combined with a strong reduction of the side lobes is shown from Fig. 2(a) towards Fig. 2(c). In Fig. 2(a), the PSF has a narrow central peak and strong side lobes. This yields excellent resolution but enhanced crosstalk levels. Moving from

Fig. 2(a) to (c) through the field-of-view, one clearly observes a gradual broadening of the central peak combined with a strong reduction of the side lobes. For PSF (c) one would observe a lower resolution but a strong suppression of optical crosstalk. This observed behavior of a field-position dependent PSF is generally undesired since optical metrology applications usually require a localized PSF that is constant across the field-of-view.

In the next section, we present a simple model of the image formation in DHM using a quasi-monochromatic light source. For the sake of clarity we use some simplifications in our model. However, despite these simplifications, we can explain the observed field-position dependent PSF. Our analysis also shows that this observation is specific for dark-field DHM and will not be observed in regular dark-field microscopy. In section 3, we then present additional experimental data that clearly shows a good match between our model and the observed field-position dependent PSF. Moreover, in this section we will also show data that explains why a field-position dependency of the PSF can have so much impact on overlay metrology. We conclude the paper by presenting some solutions to reduce the field-position dependent apodization.

2. Theory

This section presents a simple model that shows that the observed field-position dependent apodization is a consequence of the coherent detection in DHM in combination with a wavelength-dependent focal length of the imaging lens.

In our df-DHM concept the object is illuminated under an oblique angle of incidence. Part of the diffracted light is captured by the imaging lens and coherently mixed with an off-axis reference beam in the image sensor plane. The intensity on the image sensor is obtained by integrating over the source spectrum, $S(\lambda)$

$$I = \int_0^\infty S(\lambda)|O + R|^2 d\lambda, \tag{1}$$

where O and R are, respectively, the complex amplitudes of the object beam and the reference beam in the image sensor plane. Since we only consider quasi-monochromatic light, it is convenient to split λ in a central wavelength λ_c and a small difference $\Delta\lambda$ that is much smaller than λ_c,

$$\lambda = \lambda_c + \Delta\lambda. \tag{2}$$

For our off-axis df-DHM concept we only consider, from Eq. (1), the term that contains the coherent coupling between the object field O and the complex conjugate reference beam R^* since the other three terms $|O|^2$, $|R|^2$ and O^*R are removed in the signal processing. This coherent coupling term yields a complex image A_i on the image sensor plane given by

$$A_i = \int_{-\infty}^\infty S(\Delta\lambda) O R^* d\Delta\lambda, \tag{3}$$

where OR^* is cross-correlation term that describe the interference between the object and reference beam. The integration over $\Delta\lambda$ extends from $-\infty$ to ∞ but it is to be understood that the source spectrum $S(\lambda)$ is narrow ($\Delta\lambda << \lambda_c$) which bounds the actual integration limits to a very narrow range. For simplicity we describe the reference beam in our off-axis df-DHM setup as an infinite plane wave with unit amplitude that is tilted in the x-direction,

$$R = \exp[-i(k_x x + \phi_r)]. \tag{4}$$

Fourier transforming A_i, Eq. (3), and centering the resulting spectrum around the origin yields a spatial frequency spectrum A_{EP} of the complex object image,

$$\mathscr{F}\{A_i\} = A_{\mathrm{EP}} = \int_{-\infty}^\infty S(\Delta\lambda) \mathscr{F}\{O\} \exp[i\phi_r] d\Delta\lambda. \tag{5}$$

The Fourier transform $\mathscr{F}$ of the object field O is the complex field E_{EP} in the exit pupil (EP) of the imaging lens. So Eq. (5) can be expressed as,

$$A_{\mathrm{EP}} = \int_{-\infty}^{\infty} S(\Delta\lambda) E_{\mathrm{EP}} \exp[i\phi_r] d\Delta\lambda. \tag{6}$$

The PSF is measured with the use of isolated nano-scatterers [5]. For simplicity we ignore a possible angle-dependent scattering profile and we assume that the scattered light generates a uniform unit amplitude $|E_{\mathrm{E}}|$ in the exit pupil. Denoting the phase of E_p by $-\phi_o$ yields

$$A_{\mathrm{EP}} = \int_{-\infty}^{\infty} S(\Delta\lambda) \exp[i(\phi_r - \phi_o)] d\Delta\lambda. \tag{7}$$

The phase term in Eq. (7) $\phi_{ro} = \phi_r - \phi_o$ depends on $\Delta\lambda$ for two reasons:

1. An optical path difference (OPD) can exist between the object and reference beams on the camera. It has already been shown by Messinis et al. [3] that the OPD varies linearly within the field-of-view (FoV) of an off-axis dark-field DHM, as shown in Fig. 3.

   For narrow-band light ($\Delta\lambda << \lambda_c$) an OPD introduces a linear variation ϕ_{ro} with $\Delta\lambda$,

$$\phi_{ro} = a_0 \Delta\lambda. \tag{8}$$

   In appendix A we will derive an expression for the scale factor a_0.

2. The focal length of the imaging lens in DHM is wavelength-dependent which leads to a radial variation of ϕ_{ro} in the exit pupil that also scales linearly with $\Delta\lambda$,

$$\phi_{ro} = a_4 \Delta\lambda \sqrt{1 - \rho^2 \mathrm{NA}^2}, \tag{9}$$

   where ρ is the normalized radial position in the exit pupil and NA the numerical aperture of the imaging lens. In appendix B we will derive the expression for the scale factor a_4.

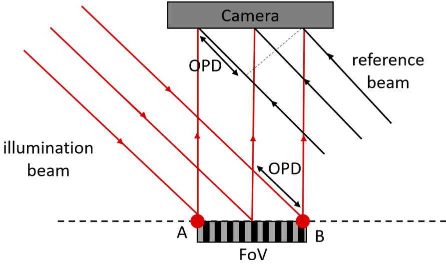

Fig. 3. The schematic representation of the illumination beam and reference beam shows that the OPD varies linearly in the FoV due to the tilted beams.

So the spatial frequency spectrum A_{EP} of the measured PSF can be written as a Fourier transform of the source spectrum,

$$A_{\mathrm{EP}}(\gamma) = \int_{-\infty}^{\infty} S(\Delta\lambda) \exp[i\gamma\Delta\lambda] d\Delta\lambda, \tag{10}$$

Optics EXPRESS

where γ is defined as,

$$\gamma = a_0 + a_4\sqrt{1 - \rho^2 \mathrm{NA}^2}. \tag{11}$$

Assuming that the shape of the beam is a narrow-band Gaussian spectrum with a $\frac{1}{e}$ bandwidth of B nm yields

$$S(\Delta\lambda) = \exp\left[-\left(\frac{2\Delta\lambda}{B}\right)^2\right]. \tag{12}$$

The spatial frequency spectrum A_{EP} is then given by,

$$A_{\mathrm{EP}}(\gamma) = \int_{-\infty}^{\infty} \exp\left[-\left(\frac{2\Delta\lambda}{B}\right)^2\right] \exp[i\gamma\Delta\lambda] d\Delta\lambda. \tag{13}$$

Evaluating the integral from Eq. (13) yields,

$$A_{\mathrm{EP}}(\gamma) = \exp\left[-\left(\frac{B}{4}\right)^2 \gamma^2\right], \tag{14}$$

with γ as defined in Eq. (11). In terms of the normalized pupil plane coordinate ρ, the spatial frequency spectrum A_{EP} of the complex object image equals,

$$A_{\mathrm{EP}}(\rho) = \exp\left[-\left(\frac{B}{4}\right)^2 \left(a_0 + a_4\sqrt{1 - \rho^2 \mathrm{NA}^2}\right)^2\right]. \tag{15}$$

Note that the above spatial frequency spectrum is a result of interference between the object and the reference beams. As a result the amplitude variations in the exit pupil plane are not present in the physical pupil plane and this also explains why this effect will not be observed in regular dark-field imaging. Some examples of pupil plane amplitude distributions A_{EP}, Eq. (15), for different values of linear dispersion a_0 and chromatic dispersion a_4 are given in Fig. 4.

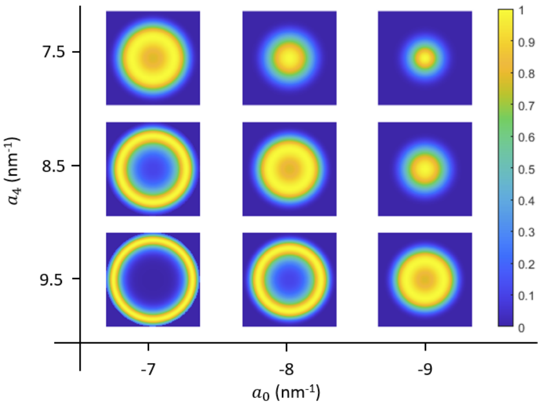

Fig. 4. A_{EP}, Eq. (15), representing the normalized pupil plane as function of a_0 and a_4 for a bandwidth of $B = 4$ nm. Realistic values of a_0 and a_4 for our dark-field DHM setup are determined using Appendix A and B.

Optics EXPRESS

3. Experimental results

In this section, we will present the experimental results of the field-position dependent apodization effect. Firstly, the df-DHM setup will be briefly described. Thereafter, the experimental results of the field-position dependent apodization using a point source are presented. In these experiments we will deliberately change the OPD in a controlled manner which allows us to validate the model that we presented in the previous section. Next, we compare the experimental data to the theoretical model presented in section 2. Finally, we present measured data to support an explanation why this field-position dependent apodization is so relevant for overlay metrology.

3.1. Experimental setup

The experimental data presented in this section is measured with our df-DHM on a breadboard setup. A schematic representation of the df-DHM setup is shown in Fig. 5. Full details of this setup are described in [4] so here we only describe the main elements of our setup. The df-DHM consists of a fiber coupled Supercontinuum White light source (LS ; Leukos Rock 400 5) combined with an acousto-optical tunable filter (AOTF). This AOTF device provides beams with a bandwidth in the range of 4 nm to 8 nm and covers the visible range of 400 nm to 700 nm. The beam intensity from the coherent white light source is split with a 90:10 beamsplitter to create an illumination and reference beam respectively. Thereafter, a 50:50 beamsplitter is used in both paths for parallel acquisition of the $+1^{st}$ and -1st diffraction orders. The light is then coupled in polarization-maintaining single-mode (PM-SM) fibers, where each reference fiber is placed on a translation stage to act as a delay line. The SM fibers transmit the light from the "light source", Fig. 5(a) to the "sensor head", Fig. 5(b). The sensor head has two off-axis illumination arms which illuminate the target from opposite directions at an incident angle of approximately 70° with respect to the normal plane of the sample. Light diffracted from the sample is then captured by the lens and imaged on the camera. At camera level the illumination beam then coherently interferes with the reference beam resulting in a digital hologram. Compared to the setup described in [4], we have replaced the off-the-shelf NA = 0.5 lens from Thorlabs by a custom-made lens with a higher NA which offers us a potentially higher imaging resolution.

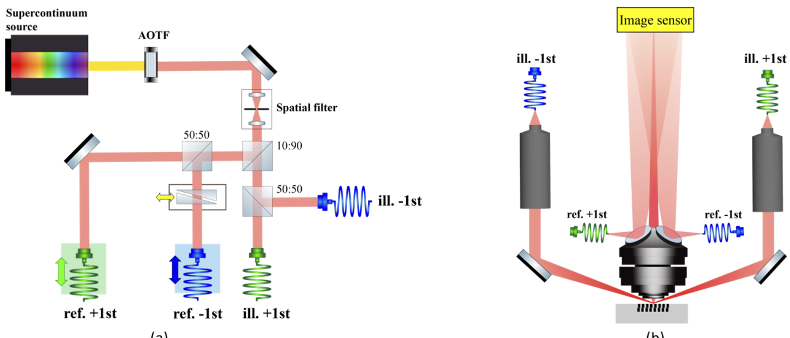

Fig. 5. A schematic representation of the experimental setup. (a) An AOTF selects the desired wavelength coming from the coherent white light source. The beam is cleaned from most of its speckle by the spatial filter, after which the beam is split in a reference and illumination beam by a 10:90 beamsplitter. 50:50 beamsplitters split the beam into two illumination and two reference beams. The two reference beam fibers are placed on a translation stage to create two delay lines. The beams are guided via polarization maintaining single mode fibers to the sensor head (b). The illumination beams are diffracted on the sample via an objective under an angle of 70°. The imaging lens catches both the $+1^{st}$ and -1st diffraction orders. The diverging reference beams are reflected via a mirror on the camera.

Optics EXPRESS

The custom made imaging lens, manufactured by Anteryon, is a high-NA lens with NA = 0.8 consisting of two lens elements fabricated from a single glass type, where one lens is an aspherical lens, Fig. 6(a). The lens is manufactured using a replication process [11,12] and is fixed in a holder on which the reference beam mirrors are integrated in such a way that the angle between reference and object beam is optimized. The nominal focal length of the Anteryon lens at 650 nm wavelength is 7.3 mm. Since the two lens elements are made of the same material a significant wavelength-dependent focus will occur, Fig. 6(b), even within the measurement bandwidth. The wavelength-dependent focus shift at a wavelength of 532 nm equals 0.7 µm/nm. To put this value in perspective, we can compare it with the Depth of Focus of this lens which equals roughly 0.8 µm at a wavelength of 532 nm.

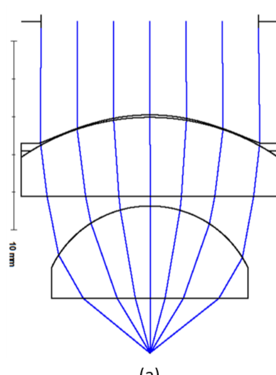

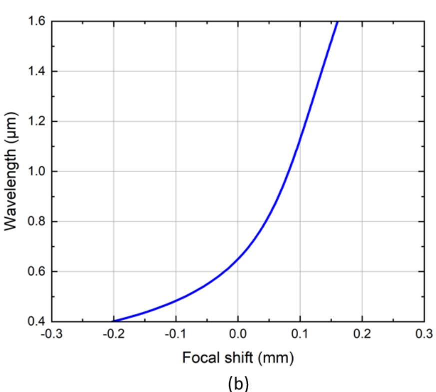

Fig. 6. (a) A schematic representation of the two element high-NA lens. (b) The longitudinal focal shift as function of the wavelength.

3.2. Field-position dependent apodization

References [2–6] report the first results that we have obtained with our dark-field DHM setup and in this paper we will report the very first measurements of the aberration-corrected PSF using the new high-NA lens in our setup. To experimentally demonstrate the field-position dependent spurious apodization, a point source illuminates the lens aperture with a spherical wave. This is done by placing a silicon sample with a nano-hole on the target position in the df-DHM. The nano-hole was manufactured using E-beam lithography resulting in a cylinder shaped hole with a diameter and depth of 100 nm. The nano-hole is then illuminated at a wavelength of 532 nm. The diffracted spherical wavefront is captured by the lens and imaged on the camera. At camera level the illumination beam interferes with the coherent reference beam resulting in a digital hologram. Fourier transforming the camera image yields the spatial frequency spectrum of the hologram. This consists of a base band term and two side bands. These two side bands are, respectively, the complex field in the exit pupil and its twin image (complex conjugate and mirrored function). By taking the absolute value of one selected side band the amplitude A_{EP} in the pupil plane is obtained. As shown in Fig. 7, translating this nano-hole point-scatterer across the FoV results in a change in amplitude distribution in the pupil plane. The light is homogeneously distributed for a point-scatterer in the center of the FoV. Whereas for the point-scatterer at the edges of the FoV the light is either centered in the pupil or spread towards the edge of the pupil as a result of change in OPD. The variation in amplitude distribution affects the PSF, which characterizes the imaging properties such as crosstalk and resolution as demonstrated in the introduction. This effect is clearly visible in a cross section of the isoplanatic aberration-corrected PSF, shown in Fig. 7. Here the isoplanatic aberrations have been corrected using the method reported in Ref. [5]. For the point source positioned at the left edge of the FoV, the light is distributed towards the

edge of the pupil resulting in enhancement of the side lobes of the PSF. Enhancing the higher spatial frequencies of the PSF increases the amount of crosstalk. Whereas for the point-scatterer at the right edge of the FoV, the light is distributed towards the center of the pupil and thereby suppresses the side lobes of the PSF (apodization). Suppressing the higher frequencies of the PSF results in less crosstalk from nearby structures. On the other hand, light filling the edges of the pupil and enhancing the side lobes results in a narrower center peak of the PSF, gaining resolution. In case of light centered in the pupil, the center peak of the PSF gets broader, which leads to a lower imaging resolution. So the position within the FoV creates a certain amount of OPD, leading to a phase shift which results in an amplitude variation.

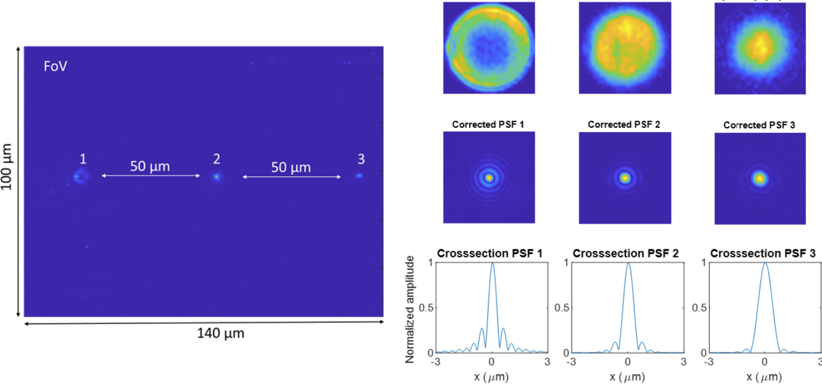

Fig. 7. The field-position dependent amplitude distribution in the pupil plane, demonstrated by translating a point-scatterer through the field-of-view, from position 1 to 3. By imaging the PSF the effect on crosstalk and resolution is shown.

The field-position dependent OPD shows how the amplitude distribution in the pupil plane affects the resolution of the imaging system and the crosstalk from nearby structures around an OV target. In the next section, we will present the bandwidth dependency of this effect. Furthermore, we use the delay line in our df-DHM setup in such a way that we can control the amplitude distribution in the pupil plane.

3.3. Controlling the amplitude variations in the pupil plane

To further investigate the OPD dependent amplitude variations in the pupil plane, two wedges (Thorlabs BSF2550) are placed in the reference beam path before coupling the light into the optical fiber, as shown in Fig. 5. Translating one of these wedges allows us to precisely tune the OPD which changes the a_0 term that we defined in section 2. In addition, we investigated the bandwidth dependency. As explained in section 2, the amplitude variation is a coherent effect. The coherence length of a source is given by $L_c = \frac{\lambda_c^2}{B}$, where λ_c is the central wavelength and B the bandwidth [13]. The bandwidth of the light and thereby the coherence length L_c can be controlled either by a laserline filter of 1 nm (Thorlabs FL532-1) or by adjusting the bandwidth with the AOTF to 4 nm or 8 nm at 532 nm wavelength. In this section, we present experimental results on the bandwidth dependency of the amplitude variations in the pupil plane by controlling the OPD with wedges. Thereby we are adjusting the linear dispersion in the DHM which equals the a_0 term from Eq. (15).

From the center position of the wedge the OPD is changed by translating one wedge. In Fig. 8, the measured normalized amplitude distributions in the pupil plane are presented as function of bandwidth and OPD. The bandwidth has been varied between 1 nm, 4 nm and 8 nm. The OPD

is in the range of 32 μm, which is of the order of magnitude as the coherence length for 8 nm bandwidth, $L_c(B = 8\,\text{nm}) = 35\,\mu\text{m}$.

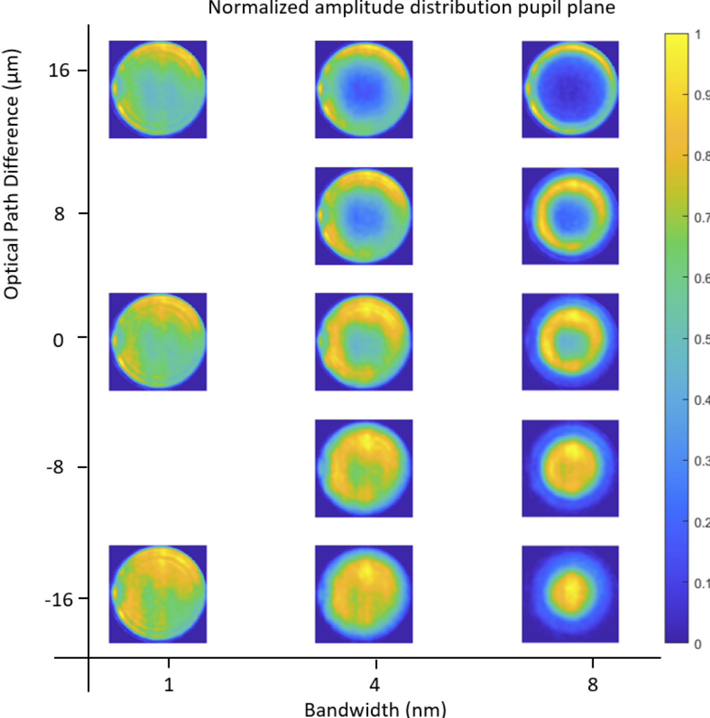

Fig. 8. The measured normalized amplitude distributions in the pupil plane as function of bandwidth and OPD. Since the change in the amplitude distribution for the 1 nm case is very gradual, no measurements were taken for the OPD = 8 and OPD = -8 points.

Analyzing the 1 nm bandwidth case, it shows that in the center position of the wedge, at OPD = 0, the amplitude is homogeneously spread over the pupil plane. Adjusting the OPD to 16 μm the light is slightly more distributed towards the edge of the pupil. However, this effect is not significantly present at an OPD of 16 μm since it is well within the coherence length of 88 μm at 1 nm bandwidth. For the 4 nm bandwidth case, the effect is more significantly visible. The results clearly show that when the OPD is lower, the light gets distributed into the center of the pupil. Whereas for higher OPDs the light gets more distributed towards the edge of the lens pupil. The amplitude variations are most clearly visible for the 8 nm bandwidth sequence. Here the OPD shift of 32 μm is of the same order of magnitude as the coherence length, $L_c(B = 8\,\text{nm}) = 35\,\mu\text{m}$. The larger the bandwidth, the more significant the OPD effect is. Moreover, for larger bandwidths, the amplitude distribution becomes donut-shaped when increasing the OPD. This shape is a result of chromatic dispersion, the a_4 term in Eq. (15), dominating the amplitude distribution.

3.4. Comparison of the theoretical model and the experimental data

To compare the experimental data presented in the previous section with the theoretical model from chapter 2, we simulated the expected amplitude distribution as function of bandwidth and OPD based on Eq. (15). The derivations of a_4 and a_0 are described in the Appendix A and B respectively. The results are presented in Fig. 9, where (a) shows the theoretical amplitude distributions, compared to the measured amplitude distributions in (b).

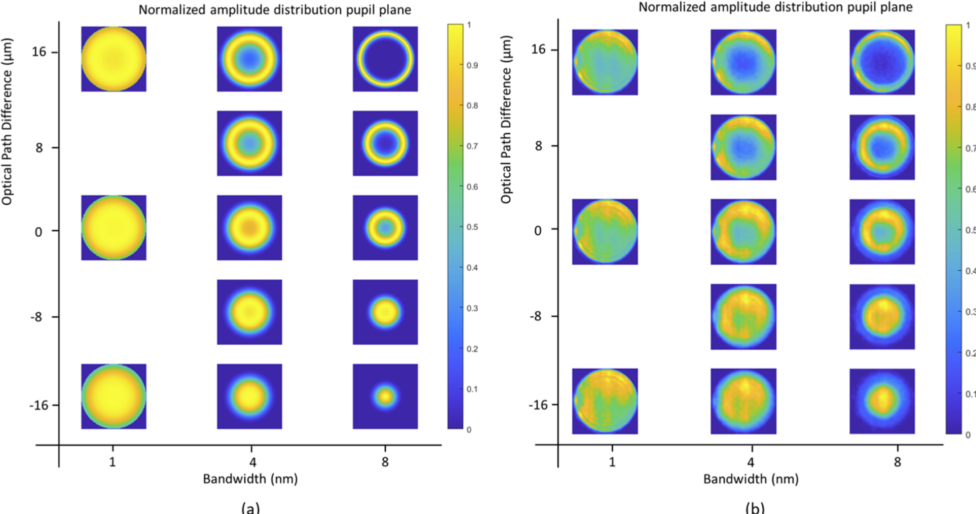

Fig. 9. The measured normalized amplitude distributions in the pupil plane as function of bandwidth and OPD, where (a) shows the simulated distributions and (b) the measured distributions.

Figure 9 clearly shows that the measurement results are in good agreement with the simple theoretical model for the three bandwidths. A closer inspection of Fig. 9 shows that there are still some deviations between our simple model and the experiments. These deviations can be explained by:

1. The theoretical model assumes that the point scatterer (nano-hole) generates a flat amplitude distribution, as described by Eq. (7). However, this is not necessarily true. Any angle-dependent scattering profile from the nano-scatterers could cause a deviation between the theoretical model and the measurements.

2. In the model we assumed a Gaussian spectrum for simplicity reasons. But in practice the real spectrum may not have a Gaussian shape.

3. The bandwidth of the source is measured with a commercial spectrometer having a resolution of 2 nm, which results in some uncertainty in the measured value for the bandwidth used in the simulation.

4. Due to Fresnel reflection losses at the edges of the two lens elements in our high-NA lens, amplitude losses at the edges of the exit pupil are expected but not covered in the theoretical model.

The four reasons described above potentially explain the small mismatch between the experimental data and the theoretical model. To improve the model we could, for example, measure the spectrum and thereby its spectral shape and bandwidth more precisely.

3.5. Relevance for overlay metrology

After having demonstrated the field-position dependent apodization, we will now show why this is relevant for a metrology application like overlay (OV) metrology. As mentioned in section 1, OV error between two semiconductor layers is measured as an intensity difference between the $+1^{st}$ and -1st diffraction orders that are diffracted by a small grating that is used as an OV metrology target. As presented in Fig. 1 and Fig. 5 these orders are generated by 2 beams that

Optics EXPRESS

illuminate the target from opposite sides at an oblique angle. Using opposite illumination beams results in an OPD variation in the image field that runs in opposite directions for the $+1^{st}$ and -1st order holograms on the camera. According to the theory presented in section 2, this results in a field-dependent spurious apodization that varies in opposite directions for the $+1^{st}$ and -1st order images. This is clearly visible in Fig. 10 which shows the measured variation of the PSF for different field positions along the x-direction. These results were obtained at a wavelength of 532 nm and a bandwidth of 8 nm. For the sake of clarity we have also included the amplitude distribution in the exit pupil that we have obtained by back-propagating the measured PSFs.

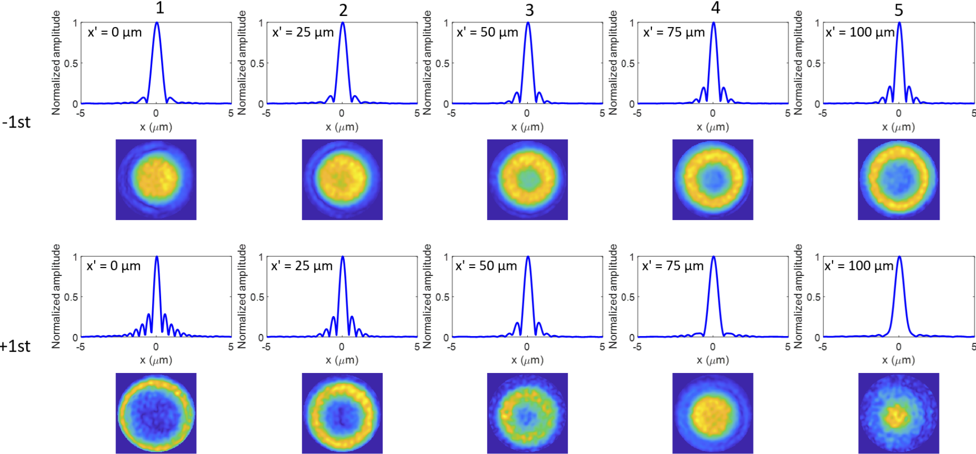

Fig. 10. Measured PSF and pupil amplitude distribution as function of position in the field for the $+1^{st}$ and -1st imaging branches in our df-DHM setup. These results were obtained at a wavelength of 532 nm and bandwidth of 8 nm.

In practice, OV targets are often surrounded by patterns like device structures or other metrology targets. These patterns also diffract the incident illumination beam resulting in a dark-field image of these patterns alongside the dark-field image of the OV target. Due to the finite resolution of the optical sensor, optical crosstalk from this adjacent pattern leaks into the image of the OV target as schematically shown in Fig. 11.

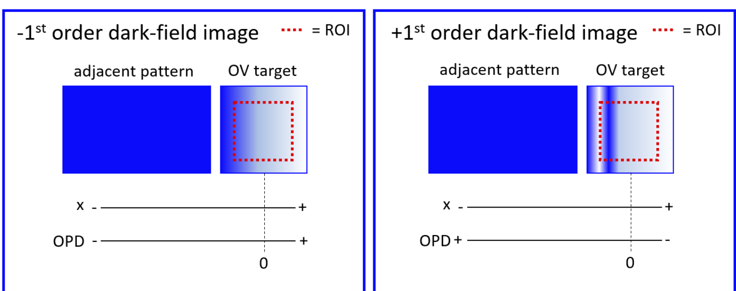

Fig. 11. Cartoon drawing of the -1st and $+1^{st}$ order images of the OV target that is adjacent to an image of a neighboring structure. For clarity, the x-direction and the direction of the OPD are indicated, showing that the OPD runs in opposite directions for the -1st and $+1^{st}$ order images. The -1st and $+1^{st}$ order signal levels that are used for the OV determination is given by the integrated signal levels in the region-of-interest (ROI) that is marked by the red dotted square.

This crosstalk will impact the measured signal level in the region-of-interest (ROI) inside the metrology target. Due to the opposite PSF variation inside the image field this impact is different for the $+1^{st}$ and -1st order images. This effect may seem small but in order to achieve sub-nanometer OV metrology precision one needs to measure intensity differences between the $+1^{st}$ and -1st diffraction order with a relative precision of the order of 10^{-4} [4]. For these extreme measurement requirements, even small variations in the PSFs can significantly affect the actual OV measurement. A proper understanding of the field-position dependency of the PSF and the possible solutions is therefore vital.

4. Proposed solutions

As presented in the previous section, the field-position dependent apodization affects the OV metrology accuracy. In order to minimize this effect or correct for its impact on the image formation, several solutions are proposed in this section. To begin with three different hardware solutions:

1. **Achromatic design with additional lens elements:** In order to compensate for the strong wavelength-dependent focal length, one could add additional lens elements to (partially) correct for a wavelength-dependent focus variation. However, adding more lens elements leads to more light losses due to reflections at the glass-air interface. Since we intend to use our DHM over a very large wavelength range from visible to shortwave infrared we cannot use anti-reflection coatings [2]. It is therefore preferred to keep the number of lens elements to an absolute minimum. More lenses lead to more glass-air interfaces which leads to more light loss and therefore lower intensity levels.

2. **Low dispersion lens material:** Another approach would be to use lens material with lower dispersion, such as CaF_2 that has an Abbe number of $V_d = 94.99$. The field-position dependent apodization will then be minimized in this case. However, such a low dispersive material generally has a low refractive index. Realizing a high-NA lens with only 2 CaF_2 lens elements would lead to unrealistically high lens curvature.

3. **Narrow bandwidth:** In this paper we presented the bandwidth dependency of the amplitude variations, showing that the broader the bandwidth the stronger the field-position dependent amplitude variations. The use of a small bandwidth is a potential hardware solution to address these field-position dependent amplitude variations. However, for best possible performance, overlay metrology needs a light source with a tunable wavelength [14–16] so a supercontinuum source is often preferred. The consequence of reducing the bandwidth with such a source is a reduction in optical power which limits the capability to measure on weak overlay targets.

From the description above it is clear that all these hardware solutions have limitations and will lead to trade-offs in terms of available optical power or achievable wavelength range. Therefore, a desired optimal solution would logically be a software correction measure, where computational correction for the field-position dependent amplitude variations in the pupil plane can be applied.

Computational correction: A software solution could be based on existing field-position dependent aberration correction algorithms [17]. Denis et al. [17] have introduced an iterative aberration correction approach for incoherent imaging in astronomy, where they refer to the field-position dependent (4D) aberrations as "shift-variant blur". Their iterative approach minimizes a least-squares cost functional for the case of the linear imaging system as it applies to incoherent imaging. The forward imaging model describes the effect of field-position dependent aberrations in terms of an efficient SVD-based decomposition of the shift-invariant blur (SVD = singular value decomposition). A similar approach could be used for our case, since the coherent imaging

regime of off-axis holography is likewise described in terms of a linear imaging system, but this the measured image field is obtained from the sideband of the hologram. The computational correction for field-position dependent apodization as addressed in our paper can be seen as a natural extension to the 4D-aberration correction approach as proposed in [17]. For that, the field-position dependent phase modulation due to the 4D-aberration function in the pupil plane will be extended with a field-position dependent amplitude modulation in the same pupil plane. This would allow a correction of the field-position dependent apodization without any hardware limitations.

5. Conclusion

In conclusion, we have demonstrated that in our df-DHM concept the finite bandwidth of the light source in combination with a wavelength-dependent focal length of the high-NA imaging lens leads to a significant field-position dependent spurious apodization that significantly affects the aberration-corrected PSF.

We have first presented field-position dependent measurements on PSFs to clarify the effect that pupil plane amplitude variations have on the crosstalk and resolution of the imaging system. Light distributed toward the edge of the pupil resulted in enhancement of the side lobes of the PSF, leading to more crosstalk and an increase in resolution. Whereas a centered amplitude distribution results in suppression of the side lobes, leading to crosstalk reduction and a lower resolution.

During the investigation we controlled the effect using wedges and thereby changing the linear dispersion in the imaging system. Moreover, we demonstrated our understanding of the observed field-position dependent apodization by comparing a simple theoretical model with experimental data. The expectations from the model matched our measurements properly with a small deviation presumably coming from the illumination spectrum not being perfectly Gaussian.

Thanks to this investigation we gained a deeper understanding of the phenomenon that impacts the image formation in our df-DHM concept. Based on our understanding and experiments we have presented an explanation why this effect is relevant for overlay metrology and we have proposed various solutions to mitigate this spurious apodization effect. We have come to the conclusion that a computational correction is the most preferred solution direction. A next step in this investigation will be to computationally correct for the amplitude variations in the pupil plane which brings us a step closer toward a df-DHM as a precise overlay metrology tool in semiconductor industry.

Appendix A. Derivation of linear dispersion a_0

The term a_0 represents the linear dispersion in our df-DHM setup. The linear dispersion originates from the delay line, the wedge and the field-position dependence. The optical path length (OPL) for, respectively, the object beam and the reference beam are given by,

$$\mathrm{OPL}_o = L_o, \tag{16}$$

$$\mathrm{OPL}_r = L_r + (n(\lambda) - 1)T_w, \tag{17}$$

where L_o and L_r are the path lengths for, respectively, the object beam and reference beam through air, T_w is the glass thickness of the tunable wedges and n is the wavelength-dependent refractive index of the wedges. The phase difference between the object and reference beam at camera level can now be described by the following equation,

$$\phi(\lambda) = \frac{2\pi}{\lambda}((n(\lambda) - 1)T_w + L_r - L_o). \tag{18}$$

Since we consider quasi monochromatic light with a central wavelength λ_c and a small wavelength variation $\Delta\lambda$ around the central wavelength: $\lambda = \lambda_c + \Delta$, we can approximate Eq. (18)

by the following linearization,

$$\phi(\lambda_c + \Delta\lambda) = 2\pi\left(\frac{1}{\lambda_c} - \frac{\Delta\lambda}{\lambda_c^2}\right)\left[\left(n_c - 1 + \frac{dn}{d\lambda}\Delta\lambda\right)T_w + L_r - L_o\right], \tag{19}$$

where n_c is the refractive index for the central wavelength λ_c. Expanding Eq. (19) and defining the tunable OPD at the central wavelength as $\text{OPD}_c = (n_c - 1)T_w + L_r - L_o$ yields,

$$\phi(\lambda_c + \Delta\lambda) = \frac{2\pi}{\lambda_c}\text{OPD}_c - \frac{2\pi}{\lambda_c}\left(\text{OPD}_c - \lambda_c T_w \frac{dn}{d\lambda}\right)\Delta\lambda - 2\pi\left(\frac{\Delta\lambda}{\lambda_c}\right)^2 \frac{dn}{d\lambda}T_w. \tag{20}$$

The last term on the right-hand side is negligibly small for the several tens of micrometers glass we add to the reference path and the bandwidth of a few nanometers that we normally consider. The 2nd term on the right-hand side of this equation is the a_0 term that gives rise to the linear dispersion:

$$a_0 = -\frac{2\pi}{\lambda_c}\left(\text{OPD}_c - \lambda_c T_w \frac{dn}{d\lambda}\right). \tag{21}$$

The a_0 term from Eq. can be tuned to 0 by either adjusting the delay line or the wedges. In this paper we adjusted the wedge which leads to a a_0 shift of 0.91 nm^{-1} when translating the wedge by 1 mm at a wavelength of 532 nm.

Appendix B. Derivation of chromatic dispersion a_4

The a_4 term represents the chromatic dispersion of the imaging lens which causes a wavelength-dependent defocus ΔF. The optical path difference (OPD) at a normalized radial position r in the exit pupil, introduced by this small defocus of the object ΔF, equals

$$\text{OPD} = \Delta F\sqrt{1 - \text{NA}^2 r^2}. \tag{22}$$

The OPD described in Eq. (22) results in a phase variation which equals,

$$\phi(\lambda) = 2\pi\frac{\text{OPD}}{\lambda}, \tag{23}$$

where λ is the wavelength. The phase shift with respect to the wavelength, can be determined by differentiating Eq. (23) yielding,

$$\frac{d\phi}{d\lambda} = 2\pi\left(\frac{1}{\lambda}\frac{d\Delta F}{d\lambda} - \frac{\Delta F}{\lambda^2}\right)\sqrt{1 - \text{NA}^2 r^2}, \tag{24}$$

where $2\pi\left(\frac{1}{\lambda}\frac{d\Delta F}{d\lambda} - \frac{\Delta F}{\lambda^2}\right)$ represents the chromatic defocus. Since the quadratic defocus term $\frac{\Delta F}{\lambda^2}$ is negligible small compared to the linear defocus term $\frac{1}{\lambda}\frac{d\Delta F}{d\lambda}$ we obtain the following Eq. for a_4

$$a_4 = 2\pi\frac{1}{\lambda_c}\frac{d\Delta F}{d\lambda}. \tag{25}$$

For the custom made high-NA imaging lens we have a wavelength-dependent focus shift of approximately 720 nm/nm at $\lambda = 532$ nm. This yields a value of $a_4 \approx 8.5\ \text{nm}^{-1}$.

Acknowledgment. We would like to thank Teus Tukker, Armand Koolen, both part of ASML Research, Marco Konijnenburg, Head Software Engineering group of AMOLF/ARCNL, and Bartjan Spaanderman, technician of Computational Imaging group of ARCNL for their support and valuable contribution to this project. We also greatfully acknowledge Rob Heeman, Klaas Paulusse, and Arthur van der Put of Anteryon for reviewing the lens description in this paper and providing information on the replication process.

Optics EXPRESS

Disclosures. The authors declare no conflicts of interest. The authors declare that they have patents or patent applications. The authors Christos Messinis, Sander Konijnenberg, Wim Coene, and Arie den Boef are employees of ASML.

Data availability. Data underlying the results presented in this paper are not publicly available at this time but may be obtained from the authors upon reasonable request.

References

1. B. Hoeneisen and C. Mead, "Fundamental limitations in microelectronics I.MOS technology," Solid-State Electron. **15**(7), 819–829 (1972).
2. T. van Schaijk, C. Messinis, N. Pandey, A. Koolen, S. Witte, J. Boer, and A. Boef, "Diffraction-based overlay metrology from visible to infrared wavelengths using a single sensor," J. Micro/Nanopatterning, Materials, and Metrology **21**(01), 014001 (2022).
3. C. Messinis, V. Tenner, J. Boer, S. Witte, and A. Boef, "Impact of coherence length on the field of view indark-field holographic microscopy for semiconductormetrology: theoretical and experimental comparisons," Appl. Opt. **59**(11), 3498 (2020).
4. C. Messinis, "Diffraction-based overlay metrology using angular-multiplexed acquisition of dark-field digital holograms," Opt. Express **28**(25), 37419–37435 (2020).
5. C. Messinis, T. van Schaijk, N. Pandey, A. Koolen, I. Shlesinger, X. Liu, S. Witte, J. Boer, and A. Boef, "Aberration calibration and correction with nano-scatterers in digital holographic microscopy for semiconductor metrology," Opt. Express **29**(23), 38237 (2021).
6. C. Messinis, M. Adhikary, T. Cromwijk, T. van Schaijk, S. Witte, J. Boer, and A. Boef, "Pupil apodization in digital holographicmicroscopy for reduction of coherent imagingeffects," Opt. Continuum **1**(5), 1202 (2022).
7. M. Kim, *Digital Holographic Microscopy: Principles, Techniques, and Applications*, Springer Series in Optical Sciences (Springer, 2011).
8. P. Leray, S. Y. Cheng, D. Kandel, M. Adel, A. Marchelli, I. Vakshtein, M. Vasconi, and B. Salski, "Diffraction based overlay metrology: accuracy and performance on front end stack," in *SPIE Advanced Lithography* (2008).
9. W. Yang, R. Lowe-Webb, S. Rabello, J. Hu, J.-Y. Lin, J. D. Heaton, M. V. Dusa, A. J. den Boef, M. van der Schaar, and A. Hunter, "Novel diffraction-based spectroscopic method for overlay metrology," in *Metrology, Inspection, and Process Control for Microlithography XVII*, vol. 5038 D. J. Herr, ed., International Society for Optics and Photonics (Proceeding SPIE, 2003), pp. 200–207.
10. M. Adel, D. Kandel, V. Levinski, J. Seligson, and A. Kuniavsky, "Diffraction order control in overlay metrology: a review of the roadmap options," in *Metrology, Inspection, and Process Control for Microlithography XXII*, vol. 6922 J. A. Allgair and C. J. Raymond, eds., International Society for Optics and Photonics (Proceeding SPIE, 2008), pp. 23–41.
11. R. J. M. Zwiers and G. C. M. Dortant, "Aspherical lenses produced by a fast high-precision replication process using uv-curable coatings," Appl. Opt. **24**(24), 4483–4488 (1985).
12. E. J. K. Verstegen, J. H. P. Faasen, H. R. Stapert, P. C. Duineveld, and J. G. Kloosterboer, "Influence of the reaction mechanism on the shape accuracy of optical components obtained by photoreplication," J. Appl. Polym. Sci. **90**(9), 2364–2376 (2003).
13. G. Fowles, *Introduction to Modern Optics* (Dover Publications, 1989), Chap. 3.
14. K. Bhattacharyya, A. den Boef, G. Storms, J. van Heijst, M. Noot, K. An, N.-K. Park, S.-R. Jeon, N.-L. Oh, E. McNamara, F. van de Mast, S. Oh, S. Y. Lee, C. Hwang, and K. Lee, "A study of swing-curve physics in diffraction-based overlay," in *Metrology, Inspection, and Process Control for Microlithography XXX*, vol. 9778 M. I. Sanchez, ed., International Society for Optics and Photonics (Proceeding SPIE, 2016), p. 97781I.
15. K. Bhattacharyya, M. Noot, H. Chang, S. Liao, K. Chang, B. Gosali, E. Su, C. Wang, A. den Boef, C. Fouquet, G.-T. Huang, K.-H. Chen, K. Cheng, and J. Lin, "Multi-wavelength approach towards on-product overlay accuracy and robustness," in *Metrology, Inspection, and Process Control for Microlithography XXXII*, vol. 10585 V. A. Ukraintsev, ed., International Society for Optics and Photonics (Proceeding SPIE, 2018), p. 105851F.
16. K. Bhattacharyya, A. den Boef, M. Noot, O. Adam, G. Grzela, A. Fuchs, M. Jak, S. Liao, K. Chang, V. Couraudon, E. Su, W. Tzeng, C. Wang, C. Fouquet, G.-T. Huang, K.-H. Chen, Y. C. Wang, K. Cheng, C.-M. Ke, and L. G. Terng, "A complete methodology towards accuracy and lot-to-lot robustness in on-product overlay metrology using flexible wavelength selection," in *Metrology, Inspection, and Process Control for Microlithography XXXI*, vol. 10145 M. I. Sanchez, ed., International Society for Optics and Photonics (Proceeding SPIE, 2017), p. 101450A.
17. L. Denis, É. Thiébaut, F. Soulez, J.-M. Becker, and R. Mourya, "Fast approximations of shift-variant blur," Int. J. Comput. Vis. **115**(3), 253–278 (2015).

192.87.153.49 {ts '2023-03-20 08:25:22'}